ISSN: 2710-0588

Preparation and Properties of CdS/SnO_2 Composite Photocatalyst

Boji Wang, Hari Bala*

Henan Polytechnic University, Jiaozuo, China

* Corresponding author

Abstract

In this paper, CdS/SnO_2 heterojunction photocatalysts with different CdS composite ratios were prepared via a hydrothermal method. Their phase structure, microstructure, specific surface area, surface chemical state, optical properties, and photocatalytic performance were systematically investigated. XRD results indicate that CdS and SnO_2 coexist in the form of a physical heterointerface without lattice doping or distortion. TEM/HRTEM and EDS analyses show that SnO_2 nanoparticles are uniformly dispersed on the surface of the CdS plate-like structure, forming a closely contacted heterointerface that facilitates efficient separation of photogenerated charge carriers. BET tests reveal that the composite possesses a mesoporous structure with a specific surface area of 23.82 m^2/g. XPS analysis confirms the existence of a built-in electric field at the heterojunction interface, consistent with type II band alignment characteristics. UV-Vis absorption spectra demonstrate that the introduction of CdS extends the photoresponse range into the visible light region, with the 0.6-CdS/SnO_2 (Cd:Sn = 3:5) sample exhibiting the strongest light absorption capability. PL and TRPL further demonstrate that this sample has the highest photogenerated carrier separation efficiency. Photocatalytic degradation experiments of Rhodamine B (RhB) show that 0.6-CdS/SnO_2 achieves a degradation rate of 93.43% within 70 min, with a reaction rate constant of 3.75×10^{-2} min^{-1}, approximately 4.88 times that of commercial P25 catalyst. Cyclic test results indicate that the composite material possesses good photocatalytic stability and reusability.

Keywords

CdS, SnO_2, composite photocatalyst, heterojunction.

1. Introduction

With the rapid development of industrialization and urbanization, the types and concentrations of organic pollutants in water and air continue to increase, posing a serious threat to the ecological environment and human health. Traditional methods such as physical adsorption and biodegradation suffer from low treatment efficiency, long cycles, and a tendency to produce secondary pollution. Photocatalytic technology has emerged as an ideal environmental remediation approach due to its simple operation, mild reaction conditions, and ability to completely mineralize organic pollutants using solar energy.

Among various photocatalytic materials, SnO_2, a wide-bandgap (approximately 3.6 eV) n-type semiconductor, possesses good chemical and thermal stability. However, its photoresponse range is mainly concentrated in the ultraviolet region, resulting in low solar light utilization, and photogenerated electron-hole pairs are prone to recombination, limiting its practical application [1-3]. CdS is a narrow-bandgap (approximately 2.4 eV) semiconductor responsive to visible light, capable of effectively absorbing visible light [4], but it suffers from strong photocorrosion and poor stability when used alone [5]. Therefore, constructing a CdS/SnO_2 heterojunction composite material has become an effective strategy. Through band matching

ISSN: 2710-0588

and the built-in electric field effect between the two semiconductors [6, 7], the spatial separation of photogenerated carriers can be promoted, recombination suppressed, the photoresponse range broadened, and photocatalytic efficiency improved [8, 9].

Currently, various methods exist for preparing CdS/SnO_2 composite materials, such as hydrothermal, sol-gel, and precipitation methods [10, 11]. Among them, the hydrothermal method features simple operation, controllable conditions, and facilitates the formation of a tight heterointerface. Previous studies have shown that CdS/SnO_2 heterojunctions exhibit good performance in the photocatalytic degradation of organic dyes [12, 13], but systematic research on the effect of the CdS composite ratio on the material structure, optical properties, and catalytic activity is still insufficient, especially regarding the interfacial charge transfer mechanism and performance optimization under different ratios.

Based on this, this paper adopts a hydrothermal method to prepare CdS/SnO_2 heterojunction composite materials with different CdS composite ratios. The crystal structure, microstructure, surface chemical state, optical absorption characteristics, and photogenerated carrier dynamics behavior are systematically investigated, and the photocatalytic degradation performance is evaluated using RhB as the target pollutant to determine the optimal CdS composite ratio. The research results provide experimental evidence and theoretical support for the design and performance regulation of efficient visible-light-driven heterojunction photocatalysts.

2. Experimental

The CdS/SnO_2 composite material was prepared by a hydrothermal method. 1 mmol of $CdCl_2 \cdot 2.5H_2O$ and 1 mmol of CN_2H_4S were added to 20 mL of deionized water and stirred thoroughly for 30 min to form a mixed solution. Then, pre-prepared SnO was added to the mixed solution at a Cd:Sn ratio of 3:5 (this ratio was determined to be optimal after multiple comparative experiments), stirred again for 30 min, transferred to a Teflon-lined autoclave, and kept at 180 °C for 24 h. After naturally cooling to room temperature, the sample was washed repeatedly with ethanol and deionized water, the precipitate collected, and dried at 60 °C for 8 h to obtain the 0.6-CdS/SnO_2 sample (0.6 represents the atomic ratio of Cd to Sn being 3:5, i.e., 0.6). For comparison, 0.4-CdS/SnO_2, 0.5-CdS/SnO_2, 0.7-CdS/SnO_2, and 0.8-CdS/SnO_2 were synthesized using the same method.

3. Results and Discussion

3.1. Phase Analysis

Figure 1 shows the X-ray diffraction patterns of SnO_2, CdS, and the CdS/SnO_2 composite material. The results indicate that upon adding cadmium chloride hemipentahydrate and thiourea, diffraction peaks related to CdS (JCPDS No. 41-1049) and SnO_2 (JCPDS No. 41-1445) are clearly observable, while the characteristic peaks of SnO completely disappear, strongly demonstrating that the SnO precursor undergoes complete oxidative phase transformation under the hydrothermal conditions at 180 °C.

Figure 2 shows the XRD patterns of CdS/SnO_2 composite materials with different CdS composite ratios, indicating that the structure of the composite does not change with different ratios. The diffraction peak positions of the samples with different ratios (0.4-0.8) show no significant shift, indicating that the introduction of CdS does not cause doping or distortion of the SnO_2 lattice; both mainly coexist in the form of a physical heterointerface. The variation in peak intensities follows the feed ratio, demonstrating the precise controllability of the hydrothermal synthesis method.

ISSN: 2710-0588

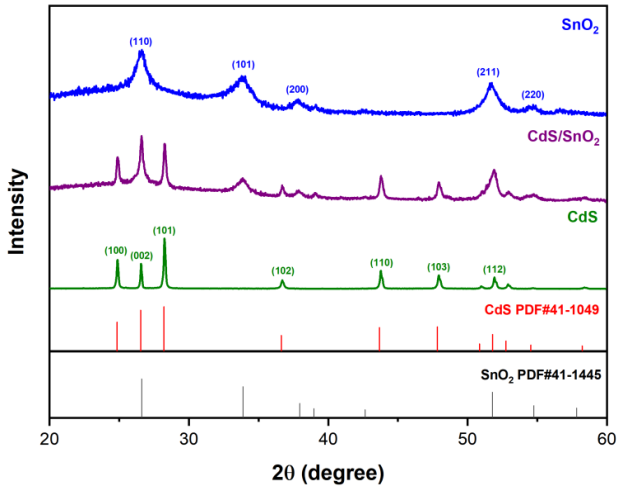

Figure 1. XRD patterns of SnO_2, CdS, and CdS/SnO_2 composite material

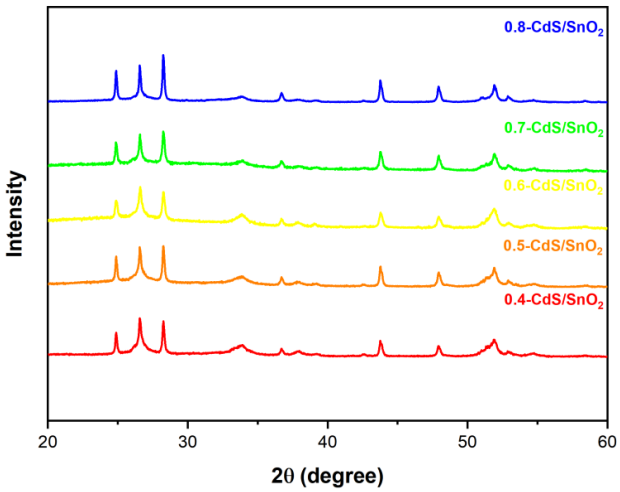

Figure 2. XRD patterns of CdS/SnO_2 composite materials with different CdS composite ratios

3.2. Microstructure Analysis

To systematically investigate the microstructure characteristics of the CdS/SnO_2 composite material, the sample was comprehensively characterized by TEM, HRTEM, and EDS, and the results are shown in Figures 3 and 4.

SEM images clearly show SnO_2 particles uniformly distributed on the CdS plate-like structure. HRTEM images clearly reveal a tight and continuous phase interface formed between CdS and SnO_2. The lattice fringe spacing of SnO_2 closely matches the standard d-value of its (110) crystal plane, confirming that the SnO precursor underwent complete phase transformation during the hydrothermal process and formed a well-crystallized SnO_2 phase. The tight bonding of CdS and SnO_2 lattices is the microstructural prerequisite for constructing an efficient cross-interface charge transport channel. This nanoscale tight heterointerface can significantly reduce the potential barrier faced by photogenerated carriers when crossing the interface, thereby promoting rapid and directional interfacial charge migration, which is the morphological basis for the excellent photocatalytic performance exhibited by the CdS/SnO_2 system.

ISSN: 2710-0588

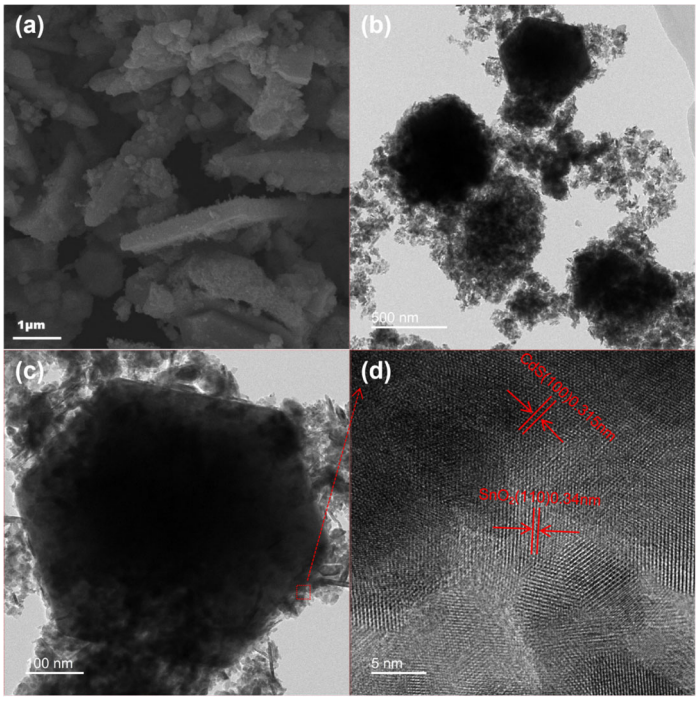

Figure 3. (a) SEM image of CdS/SnO_2 composite material, (b) and (c) TEM images of CdS/SnO_2 composite material, (e) HRTEM image of CdS/SnO_2 composite material

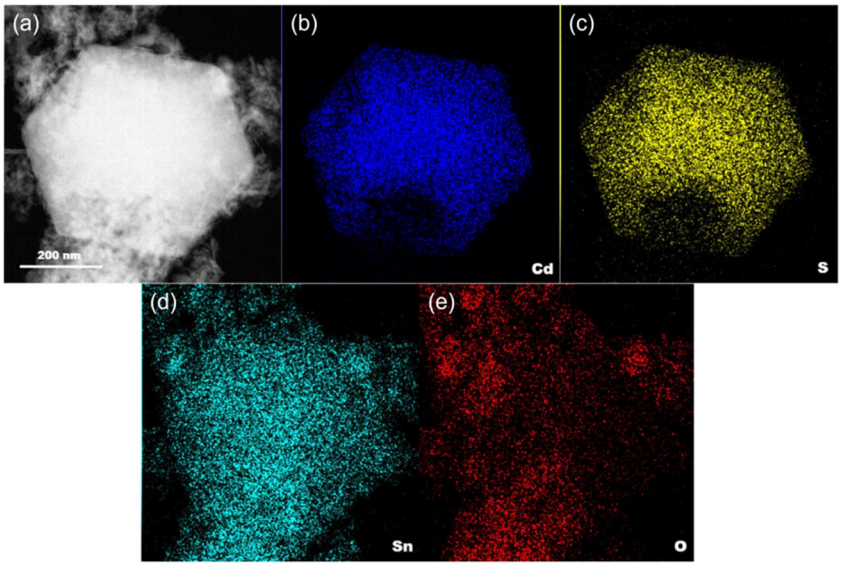

Figure 4. (a) Dark-field TEM image and elemental distribution maps of CdS/SnO_2 composite material: (b) Cd, (c) S, (d) Sn, and (e) O

To verify the successful preparation of the CdS/SnO_2 composite material, elemental analysis was performed by energy-dispersive spectroscopy, and the results are shown in Figure 4. EDS elemental mapping confirms the coexistence of Cd, Sn, S, and O elements in the composite material. The extensive and uniform distribution of Cd and S elements reflects the structural distribution characteristic of CdS serving as a uniform carrier framework in the composite, while the discrete distribution of Sn and O elements reveals the growth mode where SnO_2 nanoparticles are anchored in a dispersed state on the CdS carrier surface, confirming the successful preparation of the CdS/SnO_2 composite material.

This highly dispersed SnO_2 nanoparticle distribution not only effectively prevents the self-agglomeration of the SnO_2 phase but also significantly increases the exposure area of active

ISSN: 2710-0588

sites, thereby enhancing the effective collision frequency between the catalyst and RhB molecules, manifesting as a synergistic effect of excellent physical adsorption and chemical degradation in macroscopic photocatalytic experiments. The comprehensive characterization results from EDS, TEM, and HRTEM form a mutually corroborating and complete chain of evidence, systematically confirming the successful synthesis of the CdS/SnO_2 composite material.

3.3. Specific Surface Area and Pore Structure Analysis

To explore the structural effects of the synthesized material, the specific surface area and pore size distribution derived from nitrogen adsorption-desorption isotherms were studied using the BET and BJH methods, as shown in Figure 5.

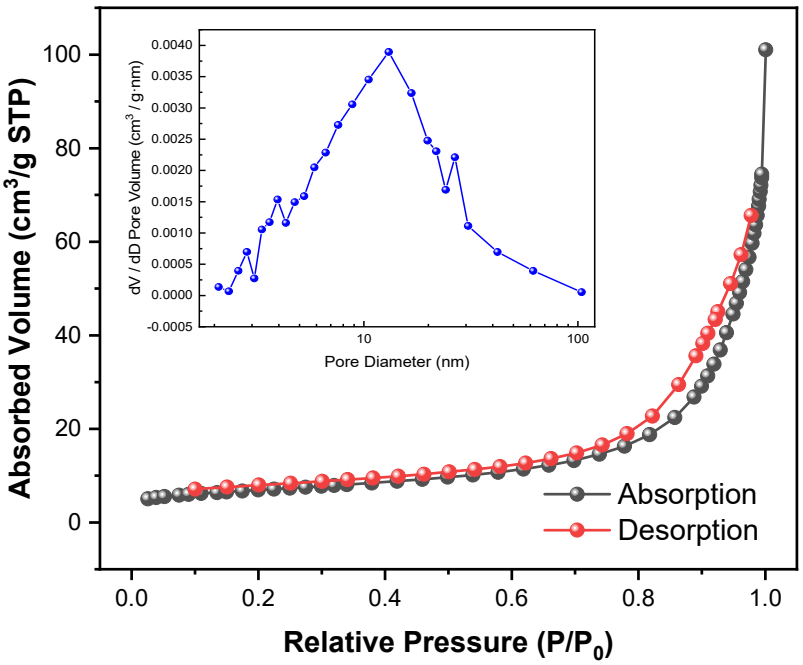

Figure.5. N_2 adsorption-desorption isotherm of the CdS/SnO_2 composite material

According to the IUPAC classification and standard isotherm type definitions, the N_2 adsorption-desorption isotherm of the prepared CdS/SnO_2 composite belongs to type III isotherm, with an H3 hysteresis loop appearing in the middle section, indicating the presence of a complex porous structure on the material's surface. The BET-calculated specific surface area of the CdS/SnO_2 composite material is 23.8219 m^2/g, pore volume is 0.1157 cm^3/g, and average pore diameter is 17.7 nm. This reflects the differential impact of the different growth habits of CdS nanoparticles on the pore structure parameters of the composite. The mesoporous structure of the CdS/SnO_2 system plays an important pre-concentration and adsorption function in photocatalytic degradation experiments, facilitating the physical adsorption of RhB molecules near the catalyst active sites before illumination, increasing the local substrate concentration for the photocatalytic reaction, and forming a synergistic enhancement basis for adsorption-assisted catalysis.

3.4. X-ray Photoelectron Spectroscopy Analysis

To determine the surface chemical composition of the synthesized product, XPS analysis was performed on the composite material, as shown in Figures 6 and 7.

ISSN: 2710-0588

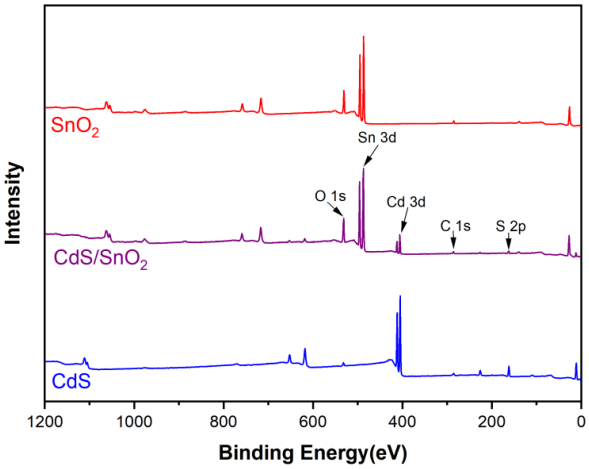

Figure 6. XPS survey spectrum of the CdS/SnO_2 composite material

In the survey spectrum of Figure 6, the main constituent elements of the composite are proven to be Cd, S, Sn, and O. Figure 7 shows the high-resolution spectra of each element in the CdS/SnO_2 composite material. Figure 7a shows two resolvable Cd 3d peaks, one attributed to Cd $3d_{5/2}$ at 404.93 eV and the other to Cd $3d_{3/2}$ photoelectron emission at 411.65 eV. Figure 7b shows the high-resolution spectrum of S 2p, with peaks at 161.43 eV and 162.69 eV, corresponding to S $2p_{3/2}$ and S $2p_{1/2}$, respectively. The two peaks in Figure 7c at 486.58 eV and 495.00 eV belong to Sn $3d_{5/2}$ and Sn $3d_{3/2}$. In the CdS/SnO_2 sample, the gap between Sn $3d_{5/2}$ and Sn $3d_{3/2}$ is 8.5 eV, consistent with the value for SnO_2. In the high-resolution O 1s spectrum shown in Figure 7d, three fitted peaks appearing at 530.49, 531.48, and 532.71 eV are assigned to lattice oxygen (O_L), oxygen vacancy (O_V), and surface-adsorbed oxygen species (O_H), respectively.

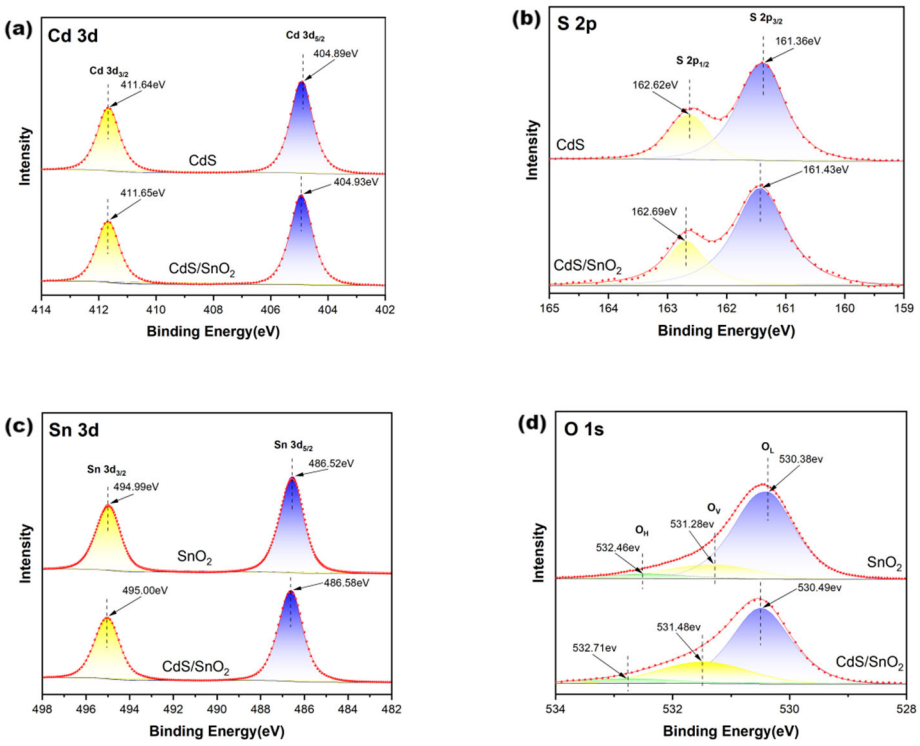

Figure 7. High-resolution XPS spectra of each element in the CdS/SnO_2 composite material

ISSN: 2710-0588

The above XPS analysis results indicate the successful synthesis of the CdS/SnO_2 composite material. The systematic shift in the binding energies of each element in the composite also confirms the existence of a built-in electric field at the CdS/SnO_2 heterojunction interface, where the Sn 3d binding energy on the SnO_2 side shifts positively (electron acceptor), while the Cd 3d and S 2p binding energies on the CdS side shift negatively (electron donor), highly consistent with the interfacial charge transfer direction under type II band alignment.

3.5. Optical and Photoelectrical Property Analysis

To investigate the influence of the CdS composite ratio on the optical properties of the CdS/SnO_2 composite material and find the optimal CdS composite ratio, four different concentrations of CdS/SnO_2 composite materials (40%, 50%, 60%, 70%, and 80%) were prepared and subjected to optical characterization tests.

Using a UV-Vis diffuse reflectance spectrometer with $BaSO_4$ as the background, the absorption spectra of the prepared series of CdS/SnO_2 composite powder samples were measured, and the results are shown in Figure 8. According to the UV-Vis absorption spectra of CdS/SnO_2 composite materials with different CdS ratios, the absorption band edge of the CdS/SnO_2 composite materials extends from 400 nm (for 0.7-CdS/SnO_2) to 340 nm (for 0.6-CdS/SnO_2), and the 0.6-CdS/SnO_2 sample exhibits the most significant advantage, possessing the strongest light absorption intensity, indicating that this sample has excellent light absorption performance and suggesting high photocatalytic activity and visible-light-induced characteristics.

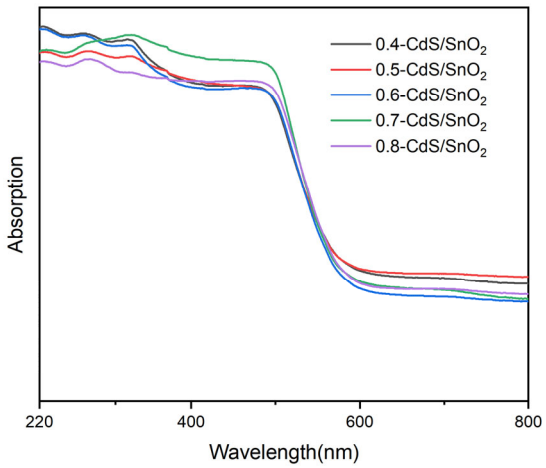

Figure 8. UV-Vis absorption spectra of CdS/SnO_2 composite materials with different ratios

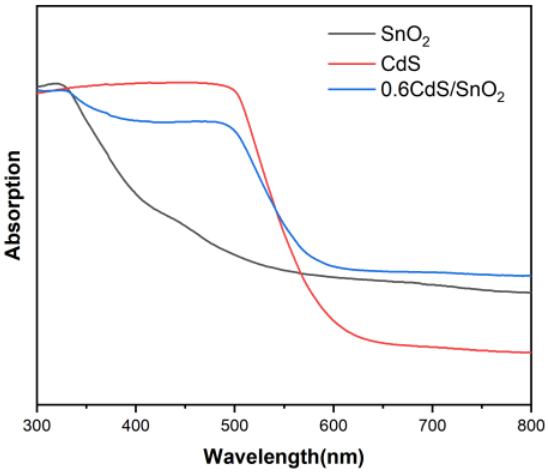

Figure 9. UV-Vis absorption spectra of SnO_2, CdS, and 0.6-CdS/SnO_2 composite material

ISSN: 2710-0588

Furthermore, to study the light absorption characteristics of each component of the CdS/SnO_2 composite material, the UV-Vis absorption spectra of SnO_2, CdS, and 0.6-CdS/SnO_2 composite were measured, as shown in Figure 9. According to the absorption spectra, SnO_2 and CdS have light absorption band edges at 330 nm and 520 nm, respectively. Pure SnO_2, as a wide-bandgap semiconductor, has its absorption band edge mainly confined to the UV region (around 330 nm), greatly limiting its utilization of the solar spectrum. After introducing CdS, the absorption edge of the composite material exhibits a significant redshift, successfully extending the photoresponse range to the visible region of 500-600 nm. This enhanced visible light absorption is attributed to the sensitization of SnO_2 by CdS, where the narrow-bandgap CdS acts as the main light absorption center.

Notably, the 0.6-CdS/SnO_2 sample exhibits the strongest absorption intensity across the entire wavelength range, indicating that at this ratio, CdS achieves optimal dispersion and loading on the SnO_2 substrate, minimizing light scattering losses.

Steady-state photoluminescence (PL) spectroscopy and time-resolved photoluminescence (TRPL) were further employed to study the dynamics of photogenerated carriers in the 0.6-CdS/SnO_2 composite material. As shown in Figure 10, the PL spectrum of the 0.6-CdS/SnO_2 composite material shows an emission peak at 830 nm. TRPL measurements were performed to measure the time decay curve of luminescence intensity after photoexcitation, studying carrier lifetime and charge separation; the measured images are shown in Figure 10. Steady-state fluorescence spectroscopy (PL) is an intuitive means of evaluating the recombination rate of photogenerated electron-hole pairs. In the composite material, 0.6-CdS/SnO_2 exhibits significant fluorescence quenching, indicating that excitons generated under photoexcitation do not release energy through radiative transitions but undergo effective charge transfer via the heterointerface. The emission peak at 830 nm may originate from defect states or metastable level transitions within the material, consistent with the oxygen vacancy distribution observed by XPS.

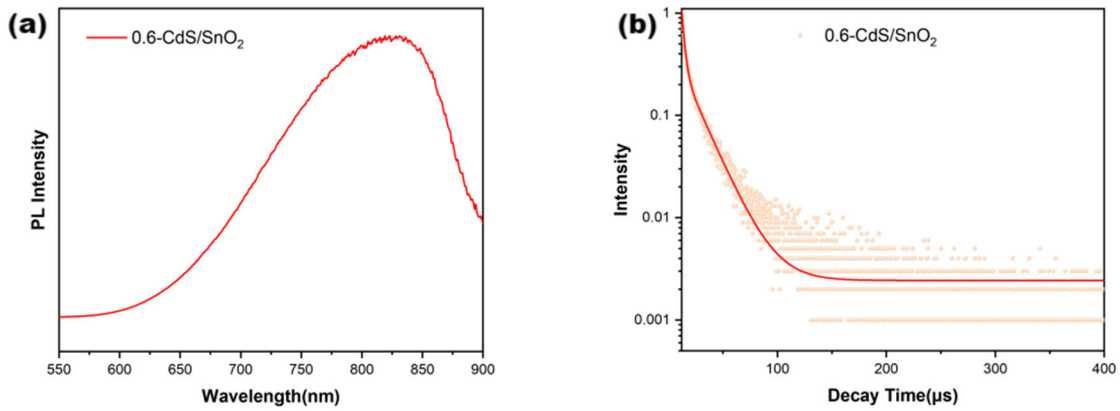

Figure 10. (a) Steady-state photoluminescence (PL) spectrum and (b) time-resolved photoluminescence (TRPL) spectrum of the 0.6-CdS/SnO_2 composite material

To quantitatively analyze the charge separation efficiency, the average lifetime (τ_{avg}) was fitted using time-resolved fluorescence spectroscopy (TRPL). Generally, the shorter fluorescence lifetime component (τ_1) in composite materials corresponds to the rapid transfer process of charges across the interface, while the longer lifetime component (τ_2) corresponds to carrier recombination in the bulk phase. The formation of the CdS/SnO_2 heterojunction alters the carrier dynamics; the shortening of the average fluorescence lifetime directly proves that the heterointerface effectively accelerates charge extraction, prolongs the survival time of

ISSN: 2710-0588

photogenerated holes on the surface, and thus endows the material with stronger oxidative degradation capability.

3.6. Evaluation of Photocatalytic Activity

The photocatalytic performance of the 0.6-CdS/SnO_2 composite material was evaluated by degrading the organic pollutant Rhodamine B (RhB) in aqueous solution. Figure 11 shows the UV-Vis absorption spectra of RhB degradation photocatalyzed by the 0.6-CdS/SnO_2 composite material under simulated solar light irradiation.

It can be seen that during the 15-minute dark reaction period, the concentration of the RhB solution significantly decreases, indicating that the prepared 0.6-CdS/SnO_2 composite material structure possesses strong physical adsorption capacity. Upon the start of the photocatalytic reaction, the absorption peak of RhB at 554 nm rapidly decreases, simultaneously shifting gradually, indicating that RhB is decomposed into secondary organic products, and finally, the absorption peak flattens, signifying the end of the decomposition process.

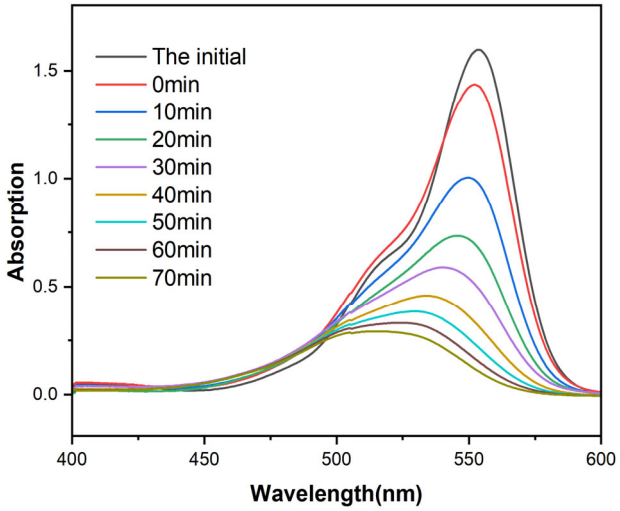

Figure 11. UV-Vis absorption spectra of RhB degradation photocatalyzed by the 0.6-CdS/SnO_2 composite material

To compare the actual impact of different CdS ratios in the composite material on the application of n-CdS/SnO_2 composite materials in the photocatalytic degradation of RhB solution, comparative tests were performed on n-CdS/SnO_2 samples with different concentrations to select the most suitable ratio. Figure 12 shows the relationship between C_t/C_0 and time, and the corresponding relationship between $\ln(C_t/C_0)$ and time, for RhB solutions under different CdS content composites at various exposure times. Figure 12(a) clearly shows the influence of different CdS composite concentrations on the system. It is evident that 0.6-CdS/SnO_2 exhibits the best catalytic rate, achieving a degradation rate of 80.46% at 40 min and 93.43% at 70 min. For further comparative analysis of reaction rates, a common pseudo-first-order kinetic equation fitting ($\ln(C_t/C_0) = kt$) was performed, where the slope k represents the reaction rate constant. From Figure 12(b), for CdS contents of 40%, 50%, 60%, 70%, and 80%, the reaction rate constants are 2.22×10^{-2}, 2.05×10^{-2}, 3.75×10^{-2}, 1.47×10^{-2}, and 1.88×10^{-2} min^{-1}, respectively. It is clear that the 60% CdS content is the best among the samples, thus determining 60% CdS composite as the optimal composite ratio.

ISSN: 2710-0588

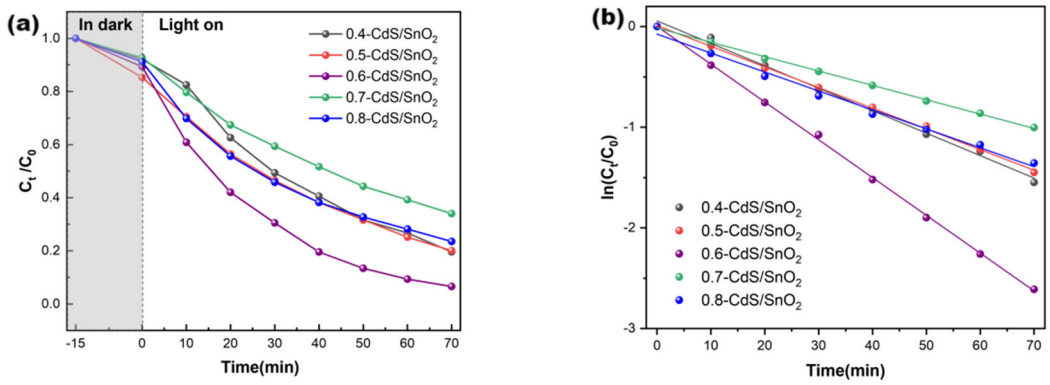

Figure 12. (a) Relationship between C_t /C_0 and time for photocatalytic degradation of RhB by CdS/SnO_2 composite materials with different concentrations; (b) Relationship between ln(C_t /C_0) and time for photocatalytic degradation of RhB by CdS/SnO_2 composite materials with different concentrations.

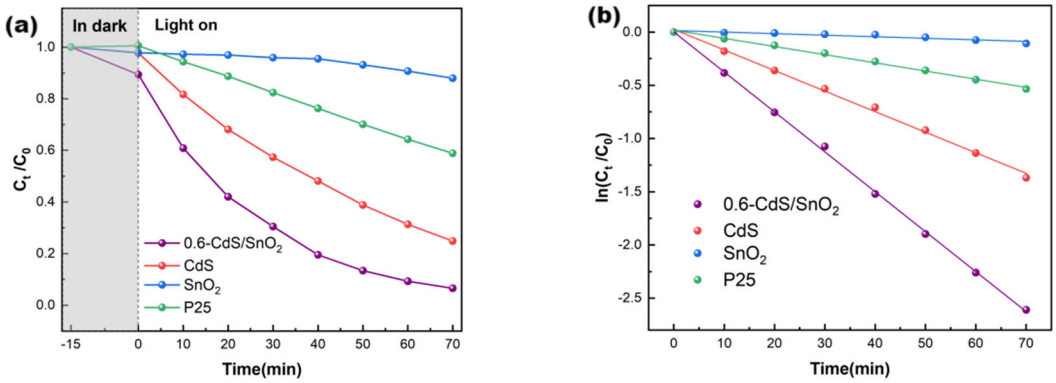

Figure 13. (a) Relationship between C_t /C_0 and time for photocatalytic degradation of RhB by P25, SnO_2, CdS, and 0.6-CdS/SnO_2 composite material; (b) Relationship between ln(C_t /C_0) and time for photocatalytic degradation of RhB by P25, SnO_2, CdS, and 0.6-CdS/SnO_2 composite material.

After determining 0.6 as the optimal ratio for the n-CdS/SnO_2 composite material, it was compared with the individual components. Commercial TiO_2 photocatalyst (P25), hydrothermally synthesized SnO_2, and hydrothermally synthesized CdS were used for comparison. Figure 13(a) shows that, compared to the commercial TiO_2 standard photocatalyst P25, as well as hydrothermally synthesized SnO_2 and CdS photocatalysts, the 0.6-CdS/SnO_2 composite material has a distinct advantage. After 70 min of catalytic reaction, P25 achieves a catalytic efficiency of 41.13%, while the 0.6-CdS/SnO_2 composite material achieves 93.43%. Figure 13(b) further shows the reaction rate constants for the photocatalytic degradation of RhB by each sample. The reaction rate constant of P25 is only 7.68×10^{-3} min^{-1}, while that of the 0.6-CdS/SnO_2 composite material can reach 3.75×10^{-2} min^{-1}, indicating that the photocatalytic activity is nearly 5 times that of P25. This demonstrates that the prepared composite photocatalyst has stronger photocatalytic activity compared to traditional P25, mainly attributed to the addition of CdS, which expands the light absorption range of the entire composite material, and the better light absorption performance enables it to better exert its performance advantages in the photocatalytic system.

ISSN: 2710-0588

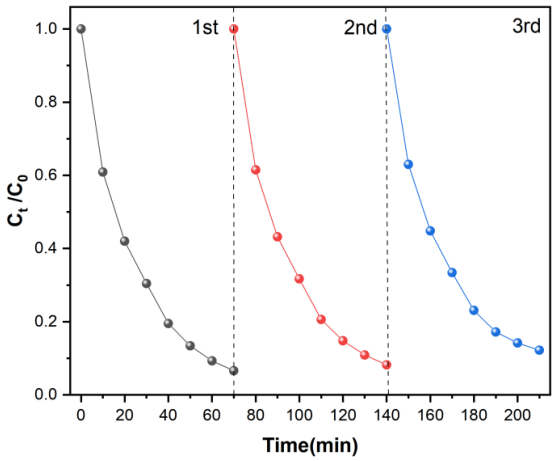

Figure 14. Cyclic catalytic test of the 0.6-CdS/SnO_2 composite material

To study the reusability and stability of the photocatalyst, repeated photocatalytic degradation tests were performed on the optimal sample, as shown in Figure 14. For each test, 100 mg of photocatalyst was used in 100 mL of RhB solution, and the degradation degree after three cycles was almost consistent. Analysis of the test results shows that with increasing cycle number, the photocatalytic efficiency of the sample decreases. In the first cycle, the catalytic efficiency reached 93.4% in 70 min; in the second cycle, the catalytic efficiency was 91.8%; in the third cycle, it was 87.8%. After 70 min of continuous degradation, the degradation efficiency could all reach above 85%. During the cyclic catalytic process, the catalytic efficiency decreases. However, considering that by the third cycle, the sample had been continuously working in water for over 3 hours, and a certain amount of photocatalyst is lost during the cyclic operation, it is judged that the decrease in efficiency is partly due to the continuous work of the catalyst causing a reduction in its inherent efficiency, and partly because the unique adsorbability of the catalyst itself prevents it from fully exerting its performance during the cycling process. Overall, after 70 min, the photocatalytic degradation efficiency can reach above 85%, fully demonstrating the reusability and photocatalytic stability of the prepared heterojunction material.

4. Conclusion

A systematic study was conducted on the hydrothermal synthesis and properties of the CdS/SnO_2 binary heterojunction composite material. The introduction of CdS significantly red-shifted the light absorption edge of the composite material from the UV region to the visible region. UV-Vis spectroscopy and Tauc plot analysis quantitatively confirmed the broad solar spectral response range of the CdS/SnO_2 system, establishing the optical material foundation for efficient visible-light-driven photocatalysis. HRTEM observed a clear and tight phase interface between CdS and SnO_2; XRD confirmed the independent coexistence of characteristic peaks of both phases without peak shift, excluding the formation of a solid solution; XPS binding energy systematic shift confirmed the existence of a built-in electric field at the CdS/SnO_2 heterojunction interface and its type II band alignment characteristics; PL and TRPL tests quantitatively characterized the enhanced carrier separation efficiency driven by the heterojunction. The multi-dimensional characterization results form a complete body of evidence. The optimal sample, 0.6-CdS/SnO_2, achieved a 93.43% degradation rate of RhB in 70 min, with a pseudo-first-order rate constant of 3.75×10^{-2} min^{-1}, approximately 4.88 times that of P25, demonstrating the efficient photocatalytic capability of the CdS/SnO_2 heterojunction system.

ISSN: 2710-0588

References

[1] Islam A, Malek A, Islam M T, et al. Next frontier in photocatalytic hydrogen production through CdS heterojunctions[J]. International Journal of Hydrogen Energy, 2025, 101: 173-211.

[2] Das S, Swain G, Parida K. A review on MXene modified quantum dot photocatalysts for sustainable energy generation and environmental remediation[J]. Catalysis Science & Technology, 2025, 15: 6976-7003.

[3] Zheng X, Liu Y, Yang Y, et al. Recent Advances in Cadmium Sulfide-Based Photocatalysts for Photocatalytic Hydrogen Evolution[J]. Renewables, 2023, 1: 39-56.

[4] Jie L, Gao X, Cao X, et al. A review of CdS photocatalytic nanomaterials: Morphology, synthesis methods, and applications[J]. Materials Science in Semiconductor Processing, 2024, 176: 108288.

[5] Milani M, Mazzanti M, Samorì C, et al. CdS-Based Hydrothermal Photocatalysts for Complete Reductive Dehalogenation of a Chlorinated Propionic Acid in Water by Visible Light[J]. Nanomaterials, 2024, 14(7): 579.

[6] Ruiz-Ortega R C, Esquivel-Mendez L A, Gonzalez-Trujillo M A, et al. Comprehensive Analysis of CdS Ultrathin Films Modified by the Substrate Position inside the Reactor Container Using the CBD Technique[J]. ACS Omega, 2023, 8(35): 31725-31737.

[7] Das C, et al. Hot-injection based synthesis of CdS and CdSe quantum dots and a comparative study of their properties[J]. AIP Conference Proceedings, 2025, 3198(1): 020010.

[8] Zhang X Y, Puttaswamy M, Bai H Q, et al. CdS/ZnS core–shell nanorod heterostructures co-deposited with ultrathin MoS_2 cocatalyst for competent hydrogen evolution under visible-light irradiation[J]. Journal of Colloid and Interface Science, 2024, 665: 430-442.

[9] Sánchez B D F ,Nair S T M ,Nair K P . Thin-film solar cells of thermally evaporated antimony sulfide selenide absorbers with ZnS–CdS window layers[J].Semiconductor Science and Technology, 2025, 40(8): 085009-085009.

[10] Li Y, Gan L H. NiS2/CdS photocatalysts with high specific surface area and excellent H_2 evolution performance[J]. International Journal of Hydrogen Energy, 2024, 60: 1500-1508.

[11] Tang Z K, Tao Y, Wang K H, et al. Lattice Mn2+ doped CdSe/CdS quantum dots for high-performance photoelectrochemical hydrogen evolution[J]. Nano Energy, 2023, 113: 108533.

[12] Xu Q, Zhang L, Cheng B, et al. S-Scheme Heterojunction Photocatalyst[J]. Chem, 2020, 6(7): 1543-1559.

[13] Ahmad I, Zhang Y, AlFaify S A, Li G, Ashraf I M, et al. Recent advances in Cd-based heterojunctions: From synthesis strategies to photocatalytic performance[J]. Journal of Alloys and Compounds, 2025, 1010: 178309.